A novel ternary plasmonic photocatalyst: ultrathin g-C$_3$N$_4$ nanosheet hybrided by Ag/AgVO$_3$ nanoribbons with enhanced visible-light photocatalytic performance

Wei Zhao, Yang Guo, Shaomang Wang, Huan He, Cheng Sun[*], Shaogui Yang[*]

State Key Laboratory of Pollution Control and Resource Reuse, School of the Environment, Nanjing University, Nanjing 210023, PR China

ARTICLE INFO

ABSTRACT

A novel Ag/AgVO$_3$/C$_3$N$_4$ ternary plasmonic photocatalyst was synthesized via a facile one-step in-situ hydrothermal method, in which the self-assembling one-dimensional (1D) AgVO$_3$ nanoribbons on the surface of two-dimensional (2D) C$_3$N$_4$ ultrathin nanosheets and Ag nanoparticles generated from AgNO$_3$ decomposition were achieved simultaneously. In this innovative hybrid structure, 1D Ag/AgVO$_3$ nanoribbons are uniformly dispersed on the surfaces of 2D C$_3$N$_4$ nanosheets. The Ag/AgVO$_3$/C$_3$N$_4$ reveals the highest photocatalytic activity for the degradation of basic fuchsin (BF) with apparent rate constant of 0.0701 min^{-1}, which is about 12.5 and 3.1 times higher than pure C$_3$N$_4$ (0.0056 min^{-1}) and Ag/AgVO$_3$ (0.0226 min^{-1}), respectively. The excellent photocatalytic performance of the ternary plasmonic photocatalyst can be attributed to the enhanced absorbance in the visible light region, the good adsorptive capacity to BF molecules, and the facilitated charge transfer in Ag/AgVO$_3$/C$_3$N$_4$. The present study will benefit the development of one new plasmonic photocatalyst and be influential in meeting the environmental demands in the future.

© 2014 Elsevier B.V. All rights reserved.

1. Introduction

Semiconductor photocatalysis is anticipated to be a green technology for environmental remediation due to its potential utilization of solar energy for purification of water and air [1–5]. Owing to its low cost, nontoxicity, and relatively high chemical stability, TiO$_2$ has proved to be the most representative and extensively used photocatalyst [6]. However, its relatively wide band gap (3.2 eV) can only respond to UV irradiation that makes up about 4% of solar energy, which greatly restricts the practical application. Therefore, numerous visible-light-driven photocatalysts with appropriate band edge positions have been designed and investigated to search for full use of solar energy [7–18].

Among the new photocatalysts under investigation, AgVO$_3$ has attracted extensive attention recently because of its narrow band gap and highly dispersed valence bands, and has been thought to be potentially useful as a visible-light-sensitive photocatalyst [19–23]. However, due to the fact that its low capability to separate electron–hole pairs limits its usage, further study is necessary to enhance its performance for the practical application.

Because the photocatalytic activity of semiconductors is structure-dependent [24–26], constructing specific morphology with excellent properties is an ideal way to enhance the performance of photocatalyst. 1D AgVO$_3$ nanoribbons with large aspect ratio and much efficient charge separation will exhibit excellent photocatalytic performances. Furthermore, the performance of the photocatalyst would be greatly improved if the surface of the semiconductor is modified with silver [27,28]. Ag, with excellent conductivity and strong electron trapping ability, can substantially increase the separation of electrons and holes between semiconductor and Ag. Moreover, the obtained Ag/semiconductor structure can exhibit strong absorbance in the visible region due to the localized surface plasmon resonance (SPR) from the collective oscillation of the surface electrons [29–33]. Some studies have shown that SPR can extend the photoresponse of catalysts and improve charge separation, which in turn enhances the catalytic performance [34–43]. For instance, Huang and coworkers [44] have fabricated a series of Ag@AgX plasmonic photocatalysts, which proved to be highly efficient and stable under visible-light illumination. Cheng et al. [45] have demonstrated that the plasmonic semiconductor nanostructures such as 2D (two-dimensional) MoO$_{3−x}$ nanosheets can be used as highly efficient

catalysts that dramatically enhance the hydrogen-generation activity of ammonia borane under visible-light irradiation. Fuku et al. [46] have reported that size- and color-controlled silver nanoparticles exhibit high catalytic activity under visible-light irradiation owing to surface plasmon resonance (SPR). More importantly, Ag/AgVO$_3$ shows highly stable photocatalytic activity under irradiation owing to the Ag particles which have already been formed and can act as photogenerated electron traps by removing electrons from the irradiated AgVO$_3$ [47].

Recently, graphitic carbon nitride (g-C$_3$N$_4$), a polymeric metal-free semiconductor with a band gap of about 2.70 eV, has been investigated focusing on the photocatalytic field [48], owing to its being a nontoxic metal-free semiconductor that possesses outstanding thermal, electrical, and optical characteristics [49]. These unique properties have attracted a great deal of scientific interest, especially its potential applications in producing hydrogen or oxygen by splitting water and degrading organic pollutants [50–52]. However, the photocatalytic efficiency of the pure g-C$_3$N$_4$ is limited by the high recombination rate of its photogenerated electron–hole pairs [53]. Therefore, it is necessary to further enhance the performance of g-C$_3$N$_4$. The successful fabrications of 2D ultrathin g-C$_3$N$_4$ nanosheets [54–56] by exfoliating their counterparts into a single atomic layer have attracted researchers' interest. These prepared 2D ultrathin g-C$_3$N$_4$ nanosheets obviously display superior properties to their bulk analogies. In addition, 2D ultrathin g-C$_3$N$_4$ nanosheets have also been recognized to be ideal candidates as catalyst carriers or promoters.

According to the above investigations, it appears that the soundest way to fabricate the highly efficient photocatalysts may be to integrate the above-mentioned merits of 1D Ag/AgVO$_3$ nanostructures and 2D ultrathin g-C$_3$N$_4$ nanosheets collectively. It is a requirement that highly efficient ternary plasmonic photocatalysts are fabricated by hybridization of these components together. However, until now, there are few reports focusing on the assembly of 1D Ag/AgVO$_3$ nanostructures with 2D g-C$_3$N$_4$ ultrathin nanosheets.

In the study, Ag/AgVO$_3$/C$_3$N$_4$ ternary plasmonic photocatalysts were synthesized by a facile one-step in-situ hydrothermal method (Scheme 1). This is the first experimental example in which the self-assembling 1D AgVO$_3$ nanoribbons on the surface of 2D C$_3$N$_4$ ultrathin nanosheets and Ag nanoparticles generated from AgNO$_3$ decomposition were achieved simultaneously.

The as-obtained Ag/AgVO$_3$/C$_3$N$_4$ ternary plasmonic photocatalyst was investigated to catalytically degrade basic fuchsin (BF, a model organic pollutant) under visible light irradiation. The mechanism for the photodegradation of BF over Ag/AgVO$_3$/C$_3$N$_4$ ternary plasmonic photocatalyst was discussed in detail. The in-situ hydrothermal synthetic strategy may open a new opportunity to develop highly efficient visible-light-driven plasmonic photocatalysts for environmental applications.

2. Materials and methods

2.1. Chemicals

Silver nitrate (AgNO$_3$), ammonium metavanadate (NH$_4$VO$_3$), melamine, and other chemicals were purchased from Shanghai Chemical Reagent Ltd., were of analytically pure grade (99%), and used without further purification. Deionized water was used throughout this study.

2.2. Preparation of 1D AgVO$_3$ and Ag/AgVO$_3$ nanoribbons

The AgVO$_3$ nanoribbons were synthesized through a facile hydrothermal process. After 20 mL of 0.050 mol/L AgNO$_3$ solution

was stirred for 30 min, 20 mL of 0.050 mol/L NH$_4$VO$_3$ solution was added, and was mixed by magnetically stirring for 180 min. The resulting mixture was transferred into a Teflon-lined stainless-steel autoclave with a volume capacity of 100 mL. This autoclave was sealed, heated to 180 °C, and maintained for 24 h. Then the system was allowed to cool to room temperature naturally. The collected product was filtrated and washed with deionized water and absolute ethanol four times, then dried under vacuum at 80 °C. 1D Ag/AgVO$_3$ nanoribbons were also constructed by the same method except for 0.055 mol/L AgNO$_3$ being added.

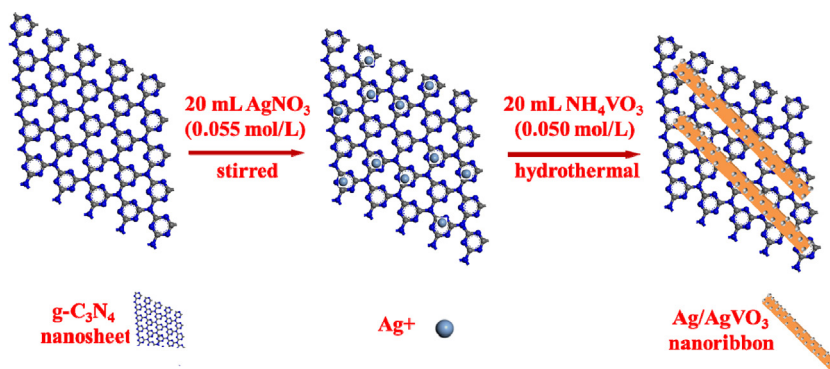### 2.3. Preparation of 2D ultrathin C$_3$N$_4$ nanosheets

The fabrication procedure of bulk g-C$_3$N$_4$ can be arranged by the thermal polycondensation of melamine [57]. In detail, 10 g of melamine was calcined at 520 °C for 4 h with the heating rate of 5 °C min^{-1}. After calcination, the received bulk g-C$_3$N$_4$ was milled into powder and heated at 550 °C for 3 h. Then, 20 mg of the obtained g-C$_3$N$_4$ was dispersed in 200 mL of 0.5 mol/L HCl at room temperature and exfoliated by ultrasonication for 8 h to prepare 2D ultrathin g-C$_3$N$_4$ nanosheets. After centrifuging and washing with deionized water, the resulting product was stirred magnetically in water for 5 h, and its pH value was adjusted to 7.0 by the addition of 0.2 mol/L NH$_4$OH solution. At last, the final product was collected by centrifugation, washed with deionized water, and dried in vacuum at 50 °C for 6 h.

2.4. Preparation of Ag/AgVO$_3$/C$_3$N$_4$ ternary plasmonic photocatalyst

The Ag/AgVO$_3$/C$_3$N$_4$ ternary plasmonic photocatalyst was synthesized through a facile one-step in-situ hydrothermal method. Briefly, 2D ultrathin g-C$_3$N$_4$ nanosheets (60 mg) were added to 20 mL of ethanol to form suspension, which was sonicated for 60 min. Then, 20 mL of 0.055 mol/L AgNO$_3$ solution was added to the suspension, which was stirred for 30 min to reach saturated adsorption of Ag$^+$ on the surface of g-C$_3$N$_4$. After that, 20 mL of 0.050 mol/L NH$_4$VO$_3$ solution was added to the suspension, which was stirred magnetically for 180 min. The resulting mixture was transferred into a Teflon-lined stainless-steel autoclave with a volume capacity of 100 mL. This autoclave was sealed, heated to 180 °C, and maintained for 24 h. The system was then allowed to cool to room temperature naturally. The collected product was filtrated and washed with deionized water and absolute ethanol four times, then dried under vacuum at 80 °C.

2.5. Photoreaction procedures

The photocatalytic activities of as-synthesized photocatalysts were evaluated by decomposing basic fuchsin (BF) under visible-light irradiation in a photoreaction apparatus. Visible light was generated by using 500 W Xe lamp irradiation with a 420 nm cut-off filter to remove light of $\lambda < 420$ nm. For photodegradation of the dye, 0.05 g of photocatalyst was put into 50 mL of 20 mg/L BF solution. Prior to irradiation, the suspension (BF solution with the photocatalyst) was magnetically stirred for 60 min to reach adsorption–desorption equilibrium in the dark. At given time intervals of visible-light irradiation, about 3 mL aliquots were collected from the reaction suspension, centrifuged at 8000 rpm for 10 min, and filtered through a 0.22 μm Millipore filter to remove the particles. The filtrates were subsequently analyzed by UV–vis spectroscopy at its maximum absorption wavelength. To ensure the reproducibility of the results, duplicate runs were made for each condition to obtain average data.

Scheme 1. Schematic of the synthesis of Ag/AgVO$_3$/C$_3$N$_4$ ternary plasmonic photocatalyst.

2.6. Characterization and calculation

X-ray diffraction (XRD) was performed at room temperature using an X'Pert-ProMPD (Holland) D/max-γA X-ray diffractometer. X-ray photo-electron spectroscopy (XPS) was used to identify surface chemical composition and chemical states of the catalysts on a PHI5000 Versa Probe electron spectrometer (ULVAC-PHI, Japan). The field emission scanning electron microscopy (FESEM) images were taken on an FEI-quanta 200F scanning electron microscope with an acceleration voltage of 20 kV. Transmission electron micrographs (TEMs) were carried out on a FEI-Tecnai F20 (200 kV) transmission electron microscope (FEI). Fluorescence emission spectra were recorded on a FluoroMax 4 type fluorescence spectrophotometer with an excitation wavelength at 350 nm. UV–vis absorption spectra were measured by using a Lambda 750 (Perkin Elmer) spectrophotometer at a wavelength range of 200–800 nm. Raman spectra were recorded with a Labram-HR confocal laser Micro-Raman spectrometer equipped with an argon ion laser.

Three-dimensional finite difference time domain (FDTD) simulations were performed to theoretically model near-field distribution of the Ag/AgVO$_3$. In the simulations, we assumed that the Ag nanoparticles with a diameter of 20 nm were uniformly distributed in the x–y-plane of the cross-section of AgVO$_3$ nanoribbon and embedded in a background medium of water. Illumination of the Ag/AgVO$_3$ was simulated with a linearly polarized plane wave, propagating in the +y-direction.

The band edge positions of both the conduction band and the valence band can be determined using a simple approach [58]. The conduction band edge (E_{CB}^0) of a semiconductor at the point of zero charge (pH$_{ZPC}$) can be predicted using the following equation:

$$E_{CB}^0 = X - E^e - 0.5E_g$$

where X is the absolute electronegativity of the semiconductor, E^e is the energy of free electrons on the hydrogen scale (4.5 eV), and E_g is the band gap of the semiconductor. The band gap energy of AgVO$_3$ is 2.1 eV. The X value for AgVO$_3$ is 5.86 eV. Consequently, the E_{CB} value of AgVO$_3$ is calculated to be 0.31 eV, and the E_{VB} value is estimated to be 2.41 eV.

3. Results and discussion

3.1. Structure and morphology of the Ag/AgVO$_3$/C$_3$N$_4$ ternary plasmonic photocatalyst

XRD was used to determine the phase structures of the as-prepared samples. As shown in Fig. 1, all the diffraction peaks can be indexed as the monoclinic β-AgVO$_3$ phase [JCPDS: 29-11541], cubic-phase Ag, and graphitic phase C$_3$N$_4$, respectively, which are marked clearly in the XRD patterns. For the Ag/AgVO$_3$ and

Ag/AgVO$_3$/C$_3$N$_4$, apart from the diffraction peaks of β-AgVO$_3$ phase, the diffraction peak at angle 38.1° is found, which can be indexed to the face-centered cubic Ag (111) phase [JCPDS card 04-0783]. No diffraction peak for the g-C$_3$N$_4$ component could be observed in Ag/AgVO$_3$/C$_3$N$_4$ due to its low percentage at the photocatalyst surface. In addition, the (501) peak of the monoclinic β-AgVO$_3$ phase is the strongest one, indicating the possible preferential orientation of the AgVO$_3$ nanoribbon.

In order to verify the existence of C$_3$N$_4$ and the chemical states of Ag species, the X-ray photoelectron spectrum (XPS) of the Ag/AgVO$_3$/C$_3$N$_4$ was measured (Fig. 2a). Chemical binding energies are observed at approximately 285.9, 400.4, 368.9, 517.9, and 532.1 eV for C 1s, N 1s, Ag 3d, V 2p, and O 1s, respectively, which suggests that the composite contains C, N, Ag, V, and O. As shown in Fig. 2b, C 1s peak at about 284.8 eV can be assigned the adventitious carbon on the surface of g-C$_3$N$_4$ and the peak at about 288.4 eV is attributed to sp^2-hybridized C (N–C=N) [59]. The N 1s peaks in Fig. 2c could be deconvoluted into two peaks, which refer to 399.4 and 401.4 eV, corresponding to N–(C)$_3$ of the g-C$_3$N$_4$ and C–N–H functional group, indicating the presence of amino groups partially. The above discussion confirms the existence of C$_3$N$_4$ in the Ag/AgVO$_3$/C$_3$N$_4$ ternary plasmonic photocatalyst. From the XPS spectra of Ag 3d (Fig. 2d), the two peaks at approximately 368.3 and 374.3 eV can be assigned to the binding energies of Ag 3d5/2 and Ag 3d3/2, respectively. These two peaks could be further deconvoluted into four bands, 368.1 and 374.1 eV for Ag+ 3d$_{5/2}$ and 3d$_{3/2}$, and 368.6 and 374.7 eV for Ag^0 3d$_{5/2}$ and 3d$_{3/2}$, which is consistent with a previous study reported by Zhu et al. [60]. The calculated Ag^0 surface mole content is about 58% in proportion to all of silver species in the catalyst surface, which verifies the existence of
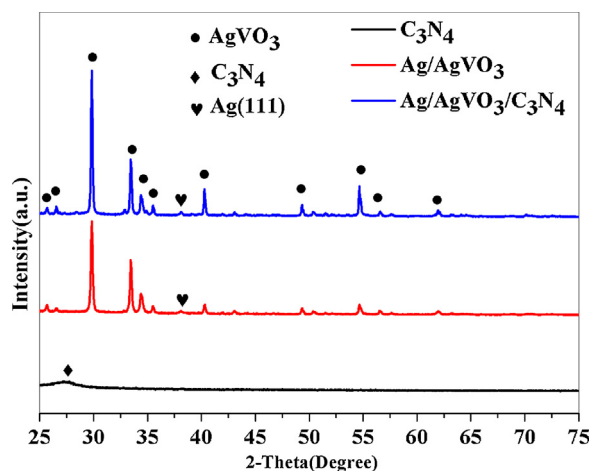

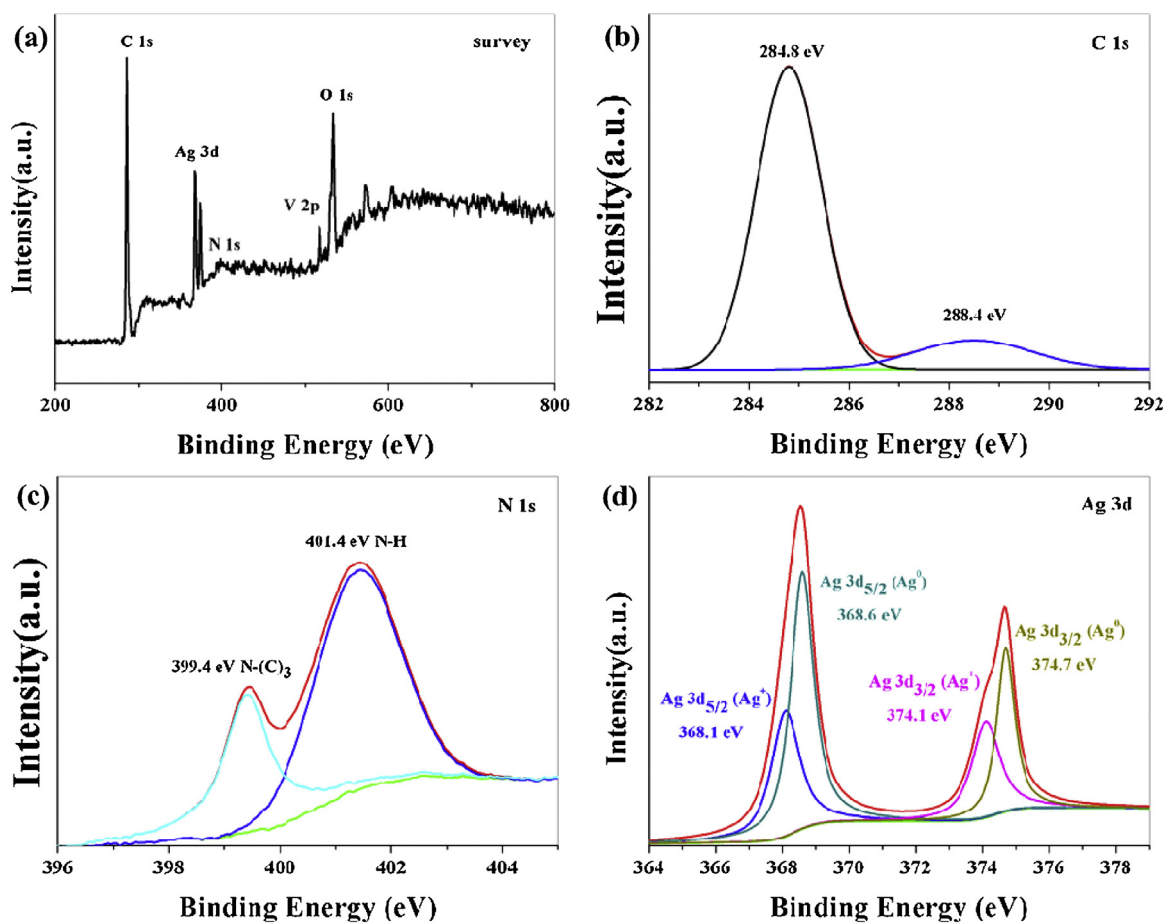**Fig. 1.** XRD patterns of the as-prepared samples.

Fig. 2. XPS spectra of (a) the survey, (b) C 1s, (c) N 1s, and (d) Ag 3d.

metallic Ag^0 in the $Ag/AgVO_3$. In addition, Fig. S1 illustrates two peaks at 517.2 and 525.1 eV, which correspond to V $2p_{5/2}$ and V $2p_{3/2}$ of V^{5+} in the $AgVO_3$, respectively.

To further understand the thickness of the C_3N_4 ultrathin nanosheet, AFM measurement was carried out. The thickness of C_3N_4 ultrathin nanosheet is only 0.6 nm (Fig. 3), which includes the interlayer distance (0.326 nm) in bulk g-C_3N_4 and a "dead layer" between the sample and the SiO_2 substrate owing to the adsorbed water [61]. The result is consistent with the single-layer g-C_3N_4 nanosheets prepared by Zhao et al. [62].

The morphologies of the as-synthesized $Ag/AgVO_3$, C_3N_4, and $Ag/AgVO_3/C_3N_4$ ternary plasmonic photocatalyst were investigated by the field emission scanning electron microscope (FESEM) and the transmission electron microscopy (TEM). Fig. S2a shows an overall view of $Ag/AgVO_3$ nanoribbons with a thickness of 50–100 nm and a width of 100–500 nm. As shown in Fig. S2b, the smooth and flat layers in the pure g-C_3N_4 nanosheets could be clearly seen, which is consistent with the reported results [63]. The crystalline structure has been confirmed by the XRD (Fig. 1) and XPS data (Fig. 2b and c). From Fig. 4a, it can be seen that two $AgVO_3$ nanoribbons with widths of about 200 nm could be obtained when C_3N_4 is not used, and many spherical Ag nanoparticles with a diameter of approximately 20–80 nm are formed on the surface of $AgVO_3$ nanoribbons. After hybrid with C_3N_4, the widths of the obtained $AgVO_3$ nanoribbons are decreased to about 30–80 nm, and a lot of Ag nanoparticles with diameters of about 10–50 nm are coated on the surface of $AgVO_3$, as shown in Fig. 4b. Furthermore, Fig. 4b clearly illustrates the lamellar structure with some chiffon-like ripples and wrinkles, which is in good accord with the characteristic layer structure of C_3N_4 sheets. The two-dimensional C_3N_4 sheets

serve as supports to load $Ag/AgVO_3$ nanowires in this ternary system. From the HRTEM image in Fig. 4c, the interplanar distances are determined to be 0.238 and 0.306 nm, which are in accordance with the *d*-spacing of the (1 1 1) crystal plane of Ag and the (5 0 1) crystal plane of $AgVO_3$, respectively [64,65]. Several one-dimensional $Ag/AgVO_3$ nanoribbons with the widths of 30–80 nm are attached on the two-dimensional C_3N_4 nanosheets and the $Ag/AgVO_3/C_3N_4$ ternary plasmonic photocatalysts are formed. On the basis of the above characterization results, $Ag/AgVO_3/C_3N_4$ ternary plasmonic photocatalysts have been successfully fabricated. Moreover, the interaction between the $Ag/AgVO_3$ nanoribbons and the C_3N_4 nanosheets is so strong that ultrasonication during the sample preparation procedure for TEM analysis could not peel off these nanoribbons.

3.2. Optical properties of the $Ag/AgVO_3/C_3N_4$ ternary plasmonic photocatalyst

The optical properties of $Ag/AgVO_3/C_3N_4$ were studied by the room-temperature fluorescence emission spectra, UV–vis absorption spectra, and Raman spectra.

The fluorescence emission spectra of the samples are shown in Fig. 5. The main emission peak is centered at about 580 nm for the pure $AgVO_3$ sample, which can be ascribed to the band gap recombination of electron–hole pairs. The emission spectrum of $AgVO_3$ has the greatest relative intensity, indicating that electrons and holes of $AgVO_3$ are easy to recombine. The relative intensity of $Ag/AgVO_3$ is lower than that of $AgVO_3$, displaying that the Ag nanoparticles formed on the surface of the $AgVO_3$ nanoribbon could partially suppress the recombination of electrons and holes.
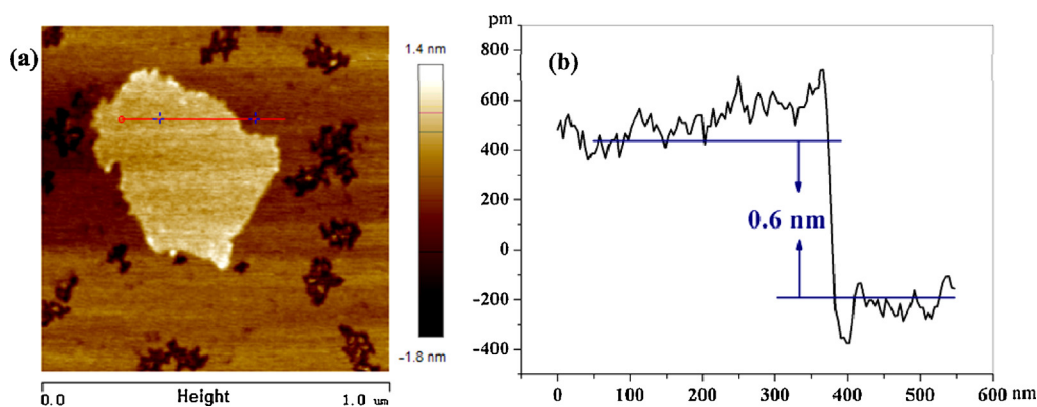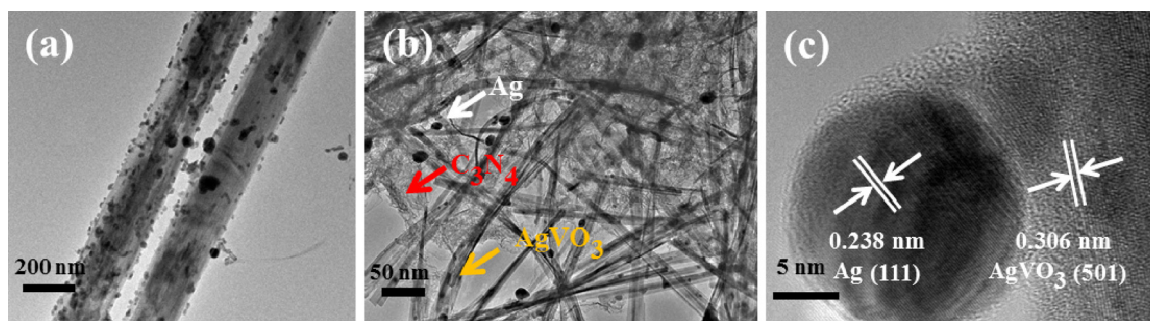
Fig. 3. AFM image of g-C_3N_4 ultrathin nanosheets.

Fig. 4. TEM image of (a) Ag/AgVO$_3$ and (b) Ag/AgVO$_3$/C$_3$N$_4$, and HRTEM image of (c) Ag/AgVO$_3$/C$_3$N$_4$.

As expected, once Ag/AgVO$_3$ is hybrided with C$_3$N$_4$ further, the relative intensity of its fluorescence emission is even lower than Ag/AgVO$_3$, which may be attributed to the efficient charge transfer between C$_3$N$_4$ and AgVO$_3$ and/or trapping of photogenerated electrons by the silver nanoparticles.

UV–vis absorption spectra of C$_3$N$_4$, AgVO$_3$, Ag/AgVO$_3$, and Ag/AgVO$_3$/C$_3$N$_4$ are illustrated in Fig. 6. The absorption edge of the pure g-C$_3$N$_4$ locates at about 460 nm, which originates from its band gap of ~2.7 eV and is consistent with the reported results [66]. Whereas the absorbance edge of AgVO$_3$ is around 590 nm, and the band-gap energy is approximately 2.1 eV. Interestingly, compared with AgVO$_3$ and Ag/AgVO$_3$, Ag/AgVO$_3$/C$_3$N$_4$ sample exhibits broad absorption in the whole visible region and its absorption intensities increase, which is attributed to SPR effect of the Ag nanoparticles formed on the surfaces of the AgVO$_3$ nanoribbons. Remarkable

absorption enhancement in the visible-light region is beneficial for improving photocatalytic activity.

Fig. 7 shows the typical Raman spectra of the as-prepared AgVO$_3$, g-C$_3$N$_4$, and Ag/AgVO$_3$/C$_3$N$_4$. By analogy with graphite, the Raman peak at about 1342 cm^{-1} for the pure g-C$_3$N$_4$ is referred to as D peak. The peaks at 680 and 981 cm^{-1} may be related to the vibration of the s-triazine rings (C$_3$N$_3$) inside the g-C$_3$N$_4$ phase. As for AgVO$_3$ sample, the strong peak at 886 cm^{-1} may originate from either bridging O-V-O or V-O-Ag vibrations. The Raman peak at 808 cm^{-1} can be associated with the stretching vibrations of the Ag-O-Ag bridges. The bridging V-O-V bond in the polymeric metavanadate chains is reflected by the 733 cm^{-1} peak, corresponding to the asymmetric stretch. The Raman peaks at 386 and 335 cm^{-1} are assigned to the symmetric and asymmetric deformation modes of the VO$_4^{-3}$ tetrahedron, respectively. Interestingly, these peak intensities of Ag/AgVO$_3$/C$_3$N$_4$ are significantly enhanced as compared with that of AgVO$_3$ nanoribbon. The enhancement of
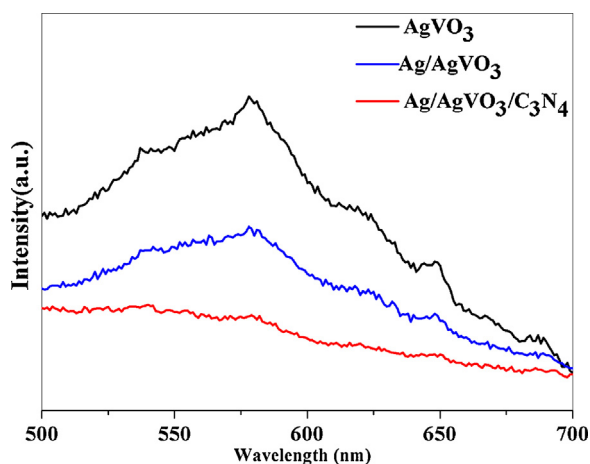

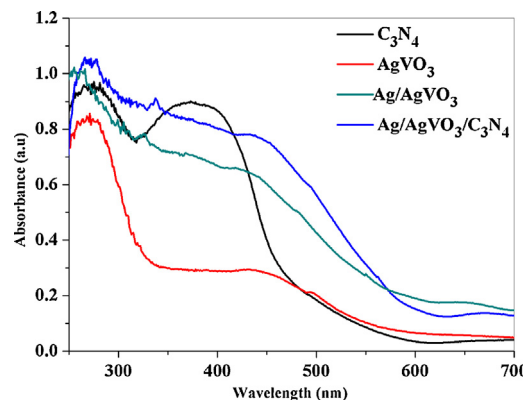**Fig. 5.** Fluorescence emission spectra of the as-prepared samples.

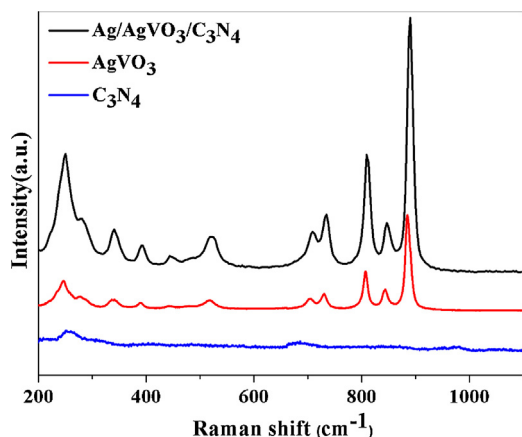**Fig. 6.** UV–vis absorption spectra of C$_3$N$_4$, AgVO$_3$, Ag/AgVO$_3$, and Ag/AgVO$_3$/C$_3$N$_4$.

Fig. 7. Raman spectra of the as-prepared AgVO$_3$, C$_3$N$_4$, and Ag/AgVO$_3$/C$_3$N$_4$ nanoribbons.

observed Raman peak intensities is similar to the surface-enhanced Raman scattering (SERS) effect previously reported [67–69]. The strong Raman enhancement in the present system may be ascribed to SPR field induced by Ag nanoparticles in Ag/AgVO$_3$/C$_3$N$_4$. It further reveals the Ag nanoparticles formed on the surfaces of the AgVO$_3$ nanoribbons, which could greatly influence electronic structure in the plasmonic photocatalytic system.

3.3. Finite-difference time-domain simulations

To explore the electric field enhancement and the SPR by the Ag nanoparticles, the electric field distribution was simulated using a three-dimensional finite-difference time domain (FDTD) method.

In the simulations, in order to simplify the procedure, the model showed in Fig. 8 is the cross-sectional view of an Ag/AgVO$_3$ nanoribbon. The cross-section was formed by cutting perpendicularly (cutting at a 90° across) to the length of the nanoribbon. As shown in Fig. 8, the local "hot spots" can be seen in regions which are among nearly touching Ag nanoparticles [70,71]. The electric field intensity at the AgVO$_3$ surface is stronger than that of the incident electromagnetic radiation under 420 nm wavelength illuminations due to SPR of the Ag nanoparticles. This influence would result in the rapid formation of electron–hole pairs near the surface of AgVO$_3$. The simulation result clearly demonstrates the occurrence of intense electric fields at the nearby AgVO$_3$ surface under 620 nm wavelength illuminations, which also explains the reason why the sample has excellent photoactivity in the visible-light region ($\lambda > 420$ nm).

Furthermore, for the composite photocatalyst, the suitable conduction band edge (E_{CB}) and valence band edge (E_{VB}) of the individual semiconductor is considered to be crucial. The E_{CB} value of AgVO$_3$ was calculated to be 0.31 eV, and the E_{VB} value was estimated to be 2.41 eV based on the Mulliken electronegativity theory. According to the previous reports [72], the lowest unoccupied molecular orbital (LUMO) and highest occupied molecular orbital (HOMO) potentials of C$_3$N$_4$ were determined to be −1.2 and 1.5 eV, respectively. Therefore, AgVO$_3$ and C$_3$N$_4$ have the suitable conduction and valence band levels for promoting charge separation at the heterojunction interfaces. Moreover, Ag nanoparticles coated on AgVO$_3$ surfaces could further facilitate charge transfer between AgVO$_3$ and Ag nanoparticles due to the relatively high conductivity and electron-storing capacity of Ag nanoparticles and induce the localized SPR that increases electric field and absorption of visible light. The results of the FDTD simulations confirm that the SPR and the electric field enhancement are caused by the Ag
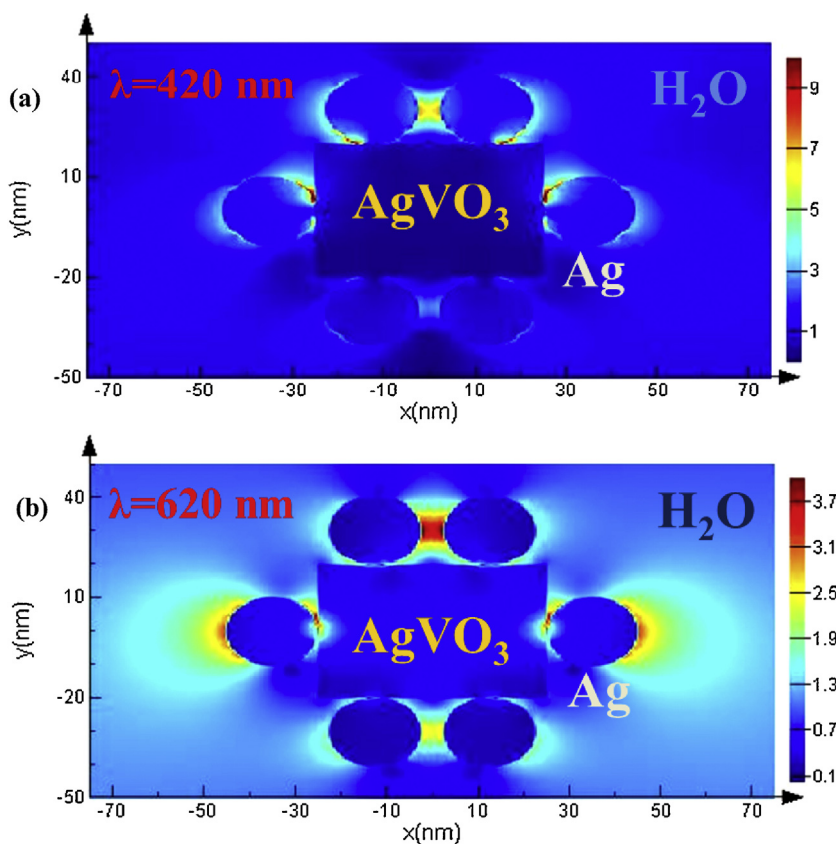

Fig. 8. Electric field distributions calculated at the cross-sections of Ag/AgVO$_3$ nanoribbons using the FDTD with light wavelengths of (a) 420 nm and (b) 620 nm. (The thickness and width of simulative AgVO$_3$ nanoribbon are 40 and 50 nm, respectively.)
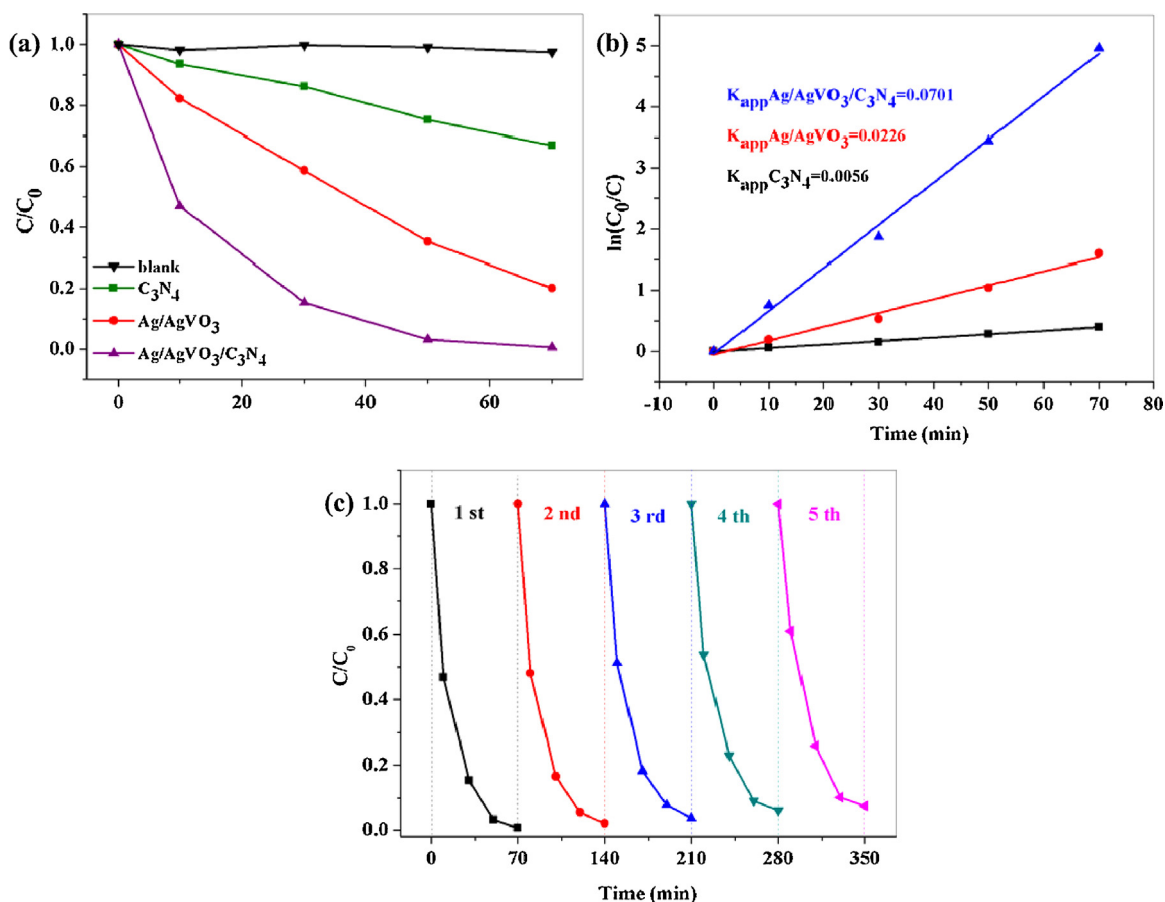
Fig. 9. (a) Photocatalytic activities and (b) pseudo-first-order kinetics of the as-prepared photocatalysts for BF degradations; (c) five recycling runs of Ag/AgVO$_3$/C$_3$N$_4$ for BF degradations.

nanoparticles. Hence, we speculate that the combination of AgVO$_3$, C$_3$N$_4$, and Ag may increase separation efficiency of electron–hole pairs and thus enhance the activity of Ag/AgVO$_3$/C$_3$N$_4$ ternary plasmonic photocatalyst.

3.4. Evaluation of photocatalytic activity

The photodegradation of basic fuchsin (BF) was carried out under visible-light irradiation to evaluate the photocatalytic activities of the samples. A dark adsorption experiment was carried out for 60 min to achieve an equilibrium adsorption state and about 22% of BF was adsorbed onto Ag/AgVO$_3$/C$_3$N$_4$. Under the

same conditions, about 5% of BF was adsorbed onto Ag/AgVO$_3$. The Ag/AgVO$_3$/C$_3$N$_4$ displayed distinctly higher adsorptive ability for BF molecules than the Ag/AgVO$_3$ (Fig. S3, dark adsorption curves).

Fig. 9a demonstrates the time dependence of BF photodegradation over the as-prepared photocatalysts under visible-light irradiation. For comparison, the performance of both pure C$_3$N$_4$, and Ag/AgVO$_3$ photocatalysts was also investigated. The blank experiment indicates that the direct photolysis of BF is almost ignored in the absence of photocatalysts. As shown in Fig. 9a, Ag/AgVO$_3$/C$_3$N$_4$ displays superior photocatalytic activity, and ~99.3% of BF molecules are degraded in just 70 min, whereas only 79.9 and 33.1% of BF molecules could be decomposed within 70 min
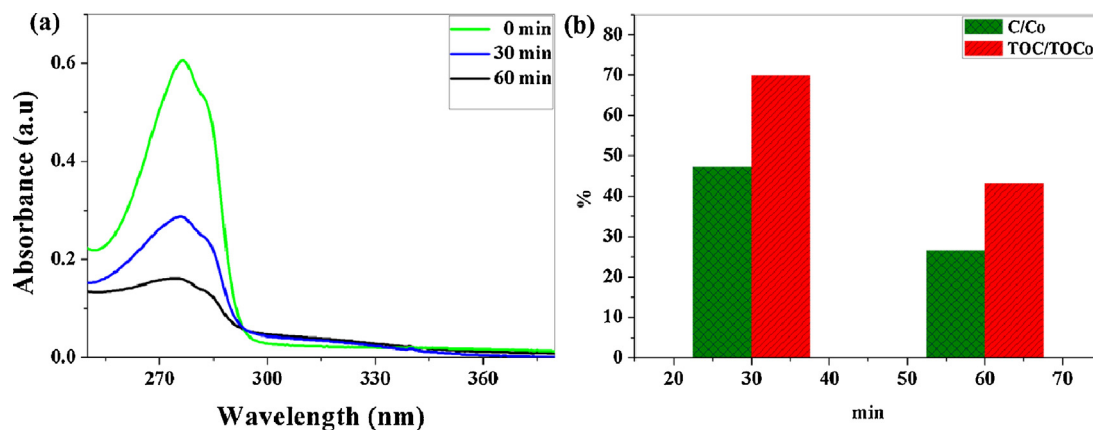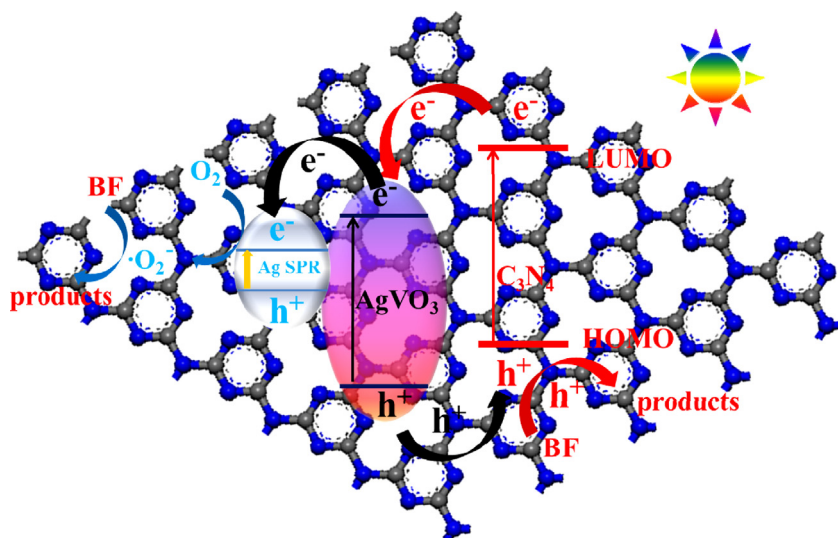

Fig. 10. (a) Temporal absorption spectral pattern, and (b) TOC removal of bisphenol A by Ag/AgVO$_3$/C$_3$N$_4$ photocatalytic degradation.

Scheme 2. Proposed mechanism of photocatalytic reaction over Ag/AgVO$_3$/C$_3$N$_4$ system.

for Ag/AgVO$_3$ and C$_3$N$_4$, respectively. It is clear that Ag/AgVO$_3$/C$_3$N$_4$ exhibits the highest photocatalytic activity among these samples. The photocatalytic degradation of BF follows a pseudo-first-order reaction and its kinetics can be expressed as $\ln(C_0/C) = k_{app}t$ [73], where C is the concentration of BF at time t, C_0 is the initial concentration of BF, and the slope k is the apparent reaction rate constant. As shown in Fig. 9b, Ag/AgVO$_3$/C$_3$N$_4$ demonstrates the highest value of k_{app} (0.0701 min^{-1}), which is about 12.5 and 3.1 times higher than that of pure C$_3$N$_4$ (0.0056 min^{-1}) and Ag/AgVO$_3$ (0.0226 min^{-1}), respectively. In addition, the stability of catalysts is an important issue for their practical applications. Therefore, the stability and the reusability of the Ag/AgVO$_3$/C$_3$N$_4$ ternary plasmonic photocatalyst during BF degradation were investigated. The ability of Ag/AgVO$_3$/C$_3$N$_4$ for the degradation of BF has barely declined, that is, after five cycling runs, about 92.5% of BF is degraded at 70 min (Fig. 9c). Obviously, the photocatalyst is stable during the photocatalytic process.

The photocatalytic performance of Ag/AgVO$_3$/C$_3$N$_4$ was also evaluated by the photodegradation of bisphenol A solution (the initial concentration of bisphenol A was 50 mg/L, the dosage of catalyst was 2.0 g/L) under visible light irradiation. Fig. 10a reveals the change of UV–vis absorption spectra of bisphenol A degradation over Ag/AgVO$_3$/C$_3$N$_4$. In order to further assess the mineralization of bisphenol A in water, total organic carbon (TOC) was also monitored during the reaction process. As shown in Fig. 10b, 56.8% of TOC is removed from the reaction system after 60 min reaction.

3.5. Discussion of the underlying mechanism of the photocatalyst

On the basis of the above-described experimental results, the mechanism of photocatalytic degradation of BF over the Ag/AgVO$_3$/C$_3$N$_4$ ternary plasmonic photocatalyst under visible-light irradiation is proposed, as illustrated in Scheme 2.

When Ag/AgVO$_3$/C$_3$N$_4$ is subjected to visible-light irradiation, plasmon-excited Ag nanoparticles, AgVO$_3$, and C$_3$N$_4$ produce photogenerated electrons and holes. Because the LUMO level of C$_3$N$_4$ (−1.2 eV) is more negative than the CB edge of AgVO$_3$ (0.31 eV), the excited electrons on the LUMO of C$_3$N$_4$ will flow into the CB of AgVO$_3$. Subsequently, the photogenerated electrons in AgVO$_3$ and those transferred from C$_3$N$_4$ could be relocated quickly towards Ag nanoparticles due to the excellent conductivity and the electron storing capacity of the Ag nanoparticles [74]. Meanwhile, photoinduced holes could migrate from the VB of AgVO$_3$ to HOMO of

C$_3$N$_4$. Thus, the photogenerated electron–hole pairs will be separated effectively by an interface formed in the Ag/AgVO$_3$/C$_3$N$_4$. Apparently, AgVO$_3$ serves as electron transfer media in the vector electron transfers of AgVO$_3$→Ag and/or C$_3$N$_4$→AgVO$_3$→Ag and then reduces the recombination possibility with photogenerated holes. Moreover, the excess electrons can be as far as possible from AgVO$_3$, instead of reducing silver ions in the AgVO$_3$, which ensures the stability of the photocatalyst. The electrons in the plasmon-excited Ag nanoparticles can be trapped by O$_2$ to form •O$_2^-$ reactive oxygen species, followed by the generation of •OH [75,76]. The photogenerated holes on C$_3$N$_4$ and Ag could then directly oxidize the dyes molecule [77,78]. The reactive species including •O$_2^-$, •OH and h$^+$ have the potential for the degradation of BF.

The explanation for the enhanced photocatalytic performance observed from the Ag/AgVO$_3$/C$_3$N$_4$ ternary plasmonic photocatalyst is proposed. First, the SPR absorption of Ag nanoparticles will remarkably enhance the absorbance of the Ag/AgVO$_3$/C$_3$N$_4$ in the visible-light region. Therefore, the formation rate of electron–hole pairs on the sample increases substantially, resulting in better catalytic performance. Second, the hybridization of C$_3$N$_4$ species in Ag/AgVO$_3$/C$_3$N$_4$ not only facilitates the adsorption of pollutant molecules, but also promotes the charge transfer between AgVO$_3$ and C$_3$N$_4$. Finally, the widths of Ag/AgVO$_3$ nanoribbons in the case of Ag/AgVO$_3$/C$_3$N$_4$ are smaller than that of bare Ag/AgVO$_3$ nanoribbons, which may also contribute partially to the enhanced photocatalytic performance.

As mentioned above, the excellent photocatalytic performance of the ternary plasmonic photocatalyst can be attributed to the enhanced absorbance in the visible-light region, the good adsorptive capacity to BF molecules, and the facilitated charge transfer in Ag/AgVO$_3$/C$_3$N$_4$.

4. Conclusions

In summary, the novel Ag/AgVO$_3$/C$_3$N$_4$ ternary plasmonic photocatalysts were synthesized by a facile one-step in-situ hydrothermal method. In these innovative hybrid structures, 1D Ag/AgVO$_3$ nanoribbons are uniformly dispersed on 2D C$_3$N$_4$ nanosheet surfaces. The as-obtained Ag/AgVO$_3$/C$_3$N$_4$ ternary plasmonic photocatalysts exhibit excellent catalytic performance, which can be ascribed to the enhanced absorbance in the visible light region, the excellent adsorptive capacity to BF molecules, and the facilitated charge transfer in Ag/AgVO$_3$/C$_3$N$_4$. The present

study will open a new opportunity to develop highly efficient visible-light-driven plasmonic photocatalysts for many environmental applications in the future.

Acknowledgements

Appendix A. Supplementary data

Supplementary data associated with this article can be found, in the online version, at http://dx.doi.org/10.1016/j.apcatb.2014.10.016.

References

[1] M.A. Shannon, P.W. Bohn, M. Elimelech, J.G. Georgiadis, B.J. Marinas, A.M. Mayes, Nature 452 (2008) 301–310.
[2] L.Q. Liu, P. Li, B. Adisak, S.X. Ouyang, N. Umezawa, J.H. Ye, R. Kodiyath, T. Tanabe, G.V. Ramesh, S. Ueda, H. Abe, J. Mater. Chem. A 2 (2014) 9415–9902.
[3] G. Liu, Y.N. Zhao, C.H. Sun, F. Li, G.Q. Lu, H.M. Cheng, Angew. Chem. Int. Ed. 120 (2008) 4592–4596.
[4] W. Zhao, Y. Jin, C.H. Gao, W. Gu, Z.M. Jin, Y.L. Lei, L.S. Liao, Mater. Chem. Phys. 143 (2014) 952–962.
[5] M. Zhang, C.C. Chen, W.H. Ma, J.C. Zhao, Angew. Chem. Int. Ed. 47 (2008) 9730–9733.
[6] S. Obregón, G. Colón, Appl. Catal. B 144 (2014) 775–782.
[7] G.M. Wang, Y.C. Ling, H.Y. Wang, X.Y. Yang, C.C. Wang, J.Z. Zhang, Y. Li, Energy Environ. Sci. 5 (2012) 6180–6187.
[8] R. Asahi, T. Morikawa, T. Ohwaki, K. Aoki, Y. Taga, Science 293 (2001) 269–271.
[9] W. Zhao, L. Feng, R. Yang, J. Zheng, X. Li, Appl. Catal. B 103 (2011) 181–189.
[10] K.S. Yang, Y. Dai, B.B. Huang, J. Phys. Chem. C 111 (2007) 18985–18994.
[11] X.B. Chen, B. Clemens, J. Am. Chem. Soc. 130 (2008) 5018–5019.
[12] J.K. Zhou, Y.X. Zhang, X.S. Zhao, A.K. Ray, Ind. Eng. Chem. Res. 45 (2006) 3503–3511.
[13] B. Peng, X.W. Meng, F.Q. Tang, X.L. Ren, D. Chen, J. Ren, J. Phys. Chem. C 113 (2009) 20240–20245.
[14] Z.G. Zou, J.H. Ye, K. Sayama, H. Arakawa, Nature 414 (2001) 625–627.
[15] D. Chen, M. Liu, Q. Chen, L. Ge, B. Fan, H. Wang, H. Lu, D. Yang, R. Zhang, Q. Yan, G. Shao, J. Sun, L. Gao, Appl. Catal. B 144 (2014) 394–407.
[16] H.L. Zhou, Y.Q. Qu, T. Zeid, X.F. Duan, Energy Environ. Sci. 5 (2012) 6732–6743.
[17] S. Zhu, S. Liang, Q. Gu, L. Xie, J. Wang, Z. Ding, P. Liu, Appl. Catal. B 119 (2012) 146–155.
[18] H.F. Cheng, B.B. Huang, Y. Dai, Nanoscale 6 (2014) 2009–2026.
[19] H. Xu, H.M. Li, L. Xu, C.D. Wu, G.S. Sun, Y.G. Xu, J.Y. Chu, Ind. Eng. Chem. Res. 48 (2009) 10771–10778.
[20] L.C. Chen, G.T. Pan, T.C.K. Yang, T.W. Chung, C.M. Huang, J. Hazard. Mater. 178 (2010) 644–651.
[21] J. Ren, W.Z. Wang, M. Shang, S.M. Sun, L. Zhang, J. Chang, J. Hazard. Mater. 183 (2010) 950–953.
[22] H.F. Shi, Z.S. Li, J.H. Kou, J.H. Ye, Z.G. Zou, J. Phys. Chem. C 115 (2011) 145–151.
[23] P. Ju, H. Fan, B.L. Zhang, K. Shang, T. Liu, S.Y. Ai, D. Zhang, Sep. Purif. Technol. 109 (2013) 107–110.
[24] S.Y. Zhang, W.Y. Li, C.S. Li, J. Chen, J. Phys. Chem. B 110 (2006) 24855–24863.
[25] S.J. Bao, Q.L. Bao, C.M. Li, T.P. Chen, C.Q. Sun, Z.L. Dong, Y. Gan, J. Zhang, Small 3 (2007) 1174–1177.
[26] J.M. Song, Y.Z. Lin, H.B. Yao, F.J. Fan, X.G. Li, S.H. Yu, ACS Nano. 3 (2009) 653–660.
[27] N. Sobana, M. Muruganadham, M. Swaminathan, J. Mol. Catal. A 258 (2006) 124–132.
[28] J. Ren, W.Z. Wang, S.M. Sun, L. Zhang, J. Chang, Appl. Catal. B 92 (2009) 50–55.
[29] M. Murdoch, G.I.N. Waterhouse, M.A. Nadeem, J.B. Metson, M.A. Keane, R.F. Howe, J. Llorca, H. Idriss, Nat. Chem. 3 (2011) 489–492.
[30] W.B. Wang, F.F. Wang, Y.R. Kang, A.Q. Wang, RSC Adv. 3 (2013) 11515–11520.
[31] Y.C. Liang, C.C. Wang, C.C. Kei, Y.C. Hsueh, W.H. Cho, T.P. Perng, J. Phys. Chem. C 115 (2011) 9498–9502.
[32] B. Zhou, X. Zhao, H.J. Liu, J.H. Qu, C.P. Huang, Sep. Purif. Technol. 77 (2011) 275–282.
[33] D.J. Wang, G.L. Xue, Y.Z. Zhen, F. Fu, D.S. Li, J. Mater. Chem. 22 (2012) 4751–4758.
[34] H. Shi, G. Li, H. Sun, T. An, H. Zhao, P.K. Wong, Appl. Catal. B 158 (2014) 301–307.
[35] B. Tian, R. Dong, J. Zhang, S. Bao, F. Yang, J. Zhang, Appl. Catal. B 158 (2014) 76–84.
[36] X. Zhang, Y. Liu, S.T. Lee, S. Yang, Z.H. Kang, Energy Environ. Sci. 7 (2014) 1409–1419.
[37] J. Gamage McEvoy, W. Cui, Z. Zhang, Appl. Catal. B 144 (2014) 702–712.
[38] C. Feng, G. Li, P. Ren, Y. Wang, X. Huang, D. Li, Appl. Catal. B 158 (2014) 224–232.
[39] J.L. Long, H.J. Chang, Q. Gu, J. Xu, L.Z. Fan, S.C. Wang, Y.G. Zhou, W. Wei, L. Huang, X.X. Wang, P. Liu, W. Huang, Energy Environ. Sci. 7 (2014) 973–977.
[40] H.F. Cheng, B.B. Huang, P. Wang, Z.Y. Wang, Z.Z. Lou, J.P. Wang, X.Y. Qin, X.Y. Zhang, Y. Dai, Chem. Commun. 47 (2011) 7054–7056.
[41] K. Mori, M. Kawashima, M. Che, H. Yamashita, Angew. Chem. 122 (2010) 8780–8783.
[42] B. Tian, T. Wang, R. Dong, S. Bao, F. Yang, J. Zhang, Appl. Catal. B 147 (2014) 22–28.
[43] X. Hu, X. Zhou, R. Wang, C. Hu, J. Qu, Appl. Catal. B 154 (2014) 44–50.
[44] P. Wang, B.B. Huang, X.Y. Qin, X.Y. Zhang, Y. Dai, J.Y. Wei, M.H. Whangbo, Angew. Chem. Int. Ed. 41 (2008) 7931–7933.
[45] H.F. Cheng, T. Kamegawa, K. Mori, H. Yamashita, Angew. Chem. Int. Ed. 53 (2014) 2910–2914.
[46] K. Fuku, R. Hayashi, S. Takakura, T. Kamegawa, K. Mori, H. Yamashita, Angew. Chem. Int. Ed. 52 (2013) 7446–7450.
[47] Z.X. Ji, M.N. Ismail, D.M. Callahan Jr., E. Pandowo, Z.H. Cai, T.L. Goodrich, K.S. Ziemer, J. Warzywoda, A. Sacco Jr., Appl. Catal. B 102 (2011) 323–333.
[48] X. Wang, K. Maeda, A. Thomas, K. Takanabe, G. Xin, J.M. Carlsson, K. Domen, M. Antonietti, Nat. Mater. 8 (2009) 76–80.
[49] J. Hu, W. Cheng, S. Huang, D. Wu, Z. Xie, Appl. Phys. Lett. 89 (2006) 261117.
[50] Q.J. Xiang, J.G. Yu, M. Jaroniec, J. Phys. Chem. C 115 (2011) 7355–7363.
[51] X. Bai, R. Zong, C. Li, D. Liu, Y. Liu, Y.F. Zhu, Appl. Catal. B 147 (2014) 82–91.
[52] S.C. Yan, Z.S. Li, Z.G. Zou, Langmuir 26 (2010) 3894–3901.
[53] G. Liu, P. Niu, C. Sun, S.C. Smith, Z. Chen, G.Q. Lu, H.M. Cheng, J. Am. Chem. Soc. 132 (2010) 11642–11648.
[54] Z. Lin, X. Wang, Angew. Chem., Int. Ed. 52 (2013) 1735–1738.
[55] P. Niu, L. Zhang, G. Liu, H.M. Cheng, Adv. Funct. Mater. 22 (2012) 4763–4770.
[56] S. Yang, Y. Gong, J. Zhang, L. Zhan, L. Ma, Z. Fang, R. Vajtai, X. Wang, P.M. Ajayan, Adv. Mater. 25 (2013) 2452–2456.
[57] G. Liao, S. Chen, X. Quan, H. Yu, H. Zhao, J. Mater. Chem. 22 (2012) 2721–2726.
[58] H. Xu, H. Li, C. Wu, J. Chu, Y. Yan, H. Shu, Z. Gu, J. Hazard. Mater. 153 (2008) 877–884.
[59] L. Ge, C.C. Han, X.L. Xiao, L.L. Guo, Appl. Catal. B 142–143 (2013) 414–422.
[60] Q. Zhu, W.S. Wang, L. Lin, G.Q. Gao, H.L. Guo, H. Du, A.W. Xu, J. Phys. Chem. C 117 (2013) 5894–5900.
[61] K.S. Novoselov, A.K. Geim, S.V. Morozov, D. Jiang, Y. Zhang, S.V. Dubonos, I.V. Grigorieva, A.A. Firsov, Science 306 (2004) 666–669.
[62] H.X. Zhao, H.T. Yu, X. Quan, S. Chen, Y.B. Zhang, H.M. Zhao, H. Wang, Appl. Catal. B 152–153 (2014) 46–50.
[63] X. Xu, G. Liu, C. Randorn, J.T.S. Irvine, Int. J. Hydrogen Energy 36 (2011) 13501–13507.
[64] S.Q. Liang, J. Zhou, X.L. Zhang, Y. Tang, G.Z. Fang, T. Chen, X.P. Tan, CrystEngComm 15 (2013) 9869–9873.
[65] M.W. Shao, L. Lu, H. Wang, S. Wang, M.L. Zhang, D.D.D. Ma, S.T. Lee, Chem. Commun. 23 (2008) 2310–2312.
[66] S.C. Yan, Z.S. Li, Z.G. Zou, Langmuir 25 (2009) 10397–10401.
[67] L. Tong, Z. Li, T. Zhu, H. Xu, Z. Liu, J. Phys. Chem. C 112 (2008) 7119–7123.
[68] Y. Kim, H. Na, Y.W. Lee, H. Jang, S.W. Han, D. Min, Chem. Commun. 46 (2010) 3185–3187.
[69] H. Zhang, X.F. Fan, X. Quan, S. Chen, H.T. Yu, Environ. Sci. Technol. 45 (2011) 5731–5736.
[70] F. Le, D.W. Brandl, Y.A. Urzhumov, H. Wang, J. Kundu, N.J. Halas, J. Aizpurua, P. Nordlander, ACS Nano 2 (2008) 707–718.
[71] W.B. Hou, Z.W. Liu, P. Pavaskar, W.H. Hung, S.B. Cronin, J. Catal. 277 (2011) 149–153.
[72] T.T. Li, L.H. Zhao, Y.M. He, J. Cai, M.F. Luo, J.J. Lin, Appl. Catal. B 129 (2013) 255–263.
[73] Y. Li, X. Li, J. Li, J. Yin, Water Res. 40 (2006) 1119–1126.
[74] Y.P. Liu, L. Fang, H.D. Lu, L.J. Liu, H. Wang, C.Z. Hu, Catal. Commun. 17 (2012) 200–204.
[75] J.G. Yu, G.P. Dai, B.B. Huang, J. Phys. Chem. C 113 (2009) 16394–16401.
[76] J.G. Yu, J.F. Xiong, B. Cheng, S.W. Liu, Appl. Catal. B 60 (2005) 211–221.
[77] X. Zhou, C. Hu, X. Hu, T. Peng, J. Qu, J. Phys. Chem. C 114 (2010) 2746–2750.
[78] P. Christopher, H.L. Xin, S. Linic, Nat. Chem. 3 (2011) 467–472.